Chapter 2
Grain Growth and Nanomaterials Behavior at High Temperatures

Abstract Current developments in kinetic and thermodynamic stabilization of grains in NMs-based metals, alloys and HMPC at high temperatures are generalized and discussed in detail. Special attention is paid to a possible quantitative estimation with using the regular solution approximation by considering both inner regions of nanograins and their interfaces. Recent data on abnormal grain growth are also considered. Practical application examples concerning bulk and film/coating objects are given and some unsolved problems are presented.

2.1 General Considerations

Many of the below described structural and functional NMs are specially destined to be used at high temperatures (for example, heat-resistant nanocomposites and tools, materials for friction assemblies and electric contacts, catalysts, emitters, sensors, etc.). For these objects, a behavior under heating accompanied by a grain growth (GG) and other processes is obviously very important. The main stimulus for grain GG is the ΔG decrease at the sacrifice of GBs component. It is known that the neighbor grains number in honeycomb-type structures with the TJs angles 120° (so-called equilibrated TJs) is equal to six and it is presumed that such structures can remain thermally stable for a very long time. Thus, the basic drive forces of GG processes are the GBs curvatures and neighbors number deviations in both sides though a growth is also connected with the GBs mobility. The theoretical description of grain growth in the usual CG materials and NMs is given by Ovid'ko in Chap. 3 of monograph [1].

In the majority of cases, CG objects are characterized by a cooperative homogeneous grain displacement and merging when their lognormal or normal GS distributions preserve (Fig. 2.1b). In NMs grain growth proceeds owing to their rotation as well (Fig. 2.1c). Also, an abnormal grain growth is observed which is accompanied with the appearance of CG seats or centers absorbing their smaller neighbors as it is in Fig. 2.2 with possible formation of a new bimodal GS distribution. Such abnormal grain growth is also characteristic in some NMs produced by

R.A. Andrievski and A.V. Khatchoyan, *Nanomaterials in Extreme Environments*,
Springer Series in Materials Science 230, DOI 10.1007/978-3-319-25331-2_2

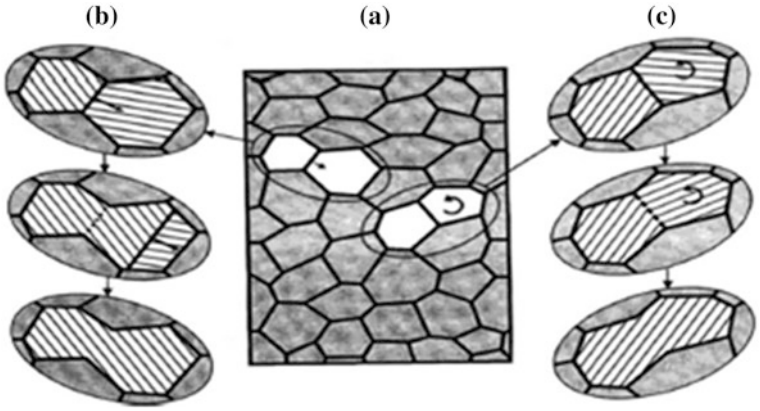

Fig. 2.1 Scheme of grain growth: **a** Initial state. **b** Migration and boundary merging. **c** Rotation and boundary merging (adapted from [1])

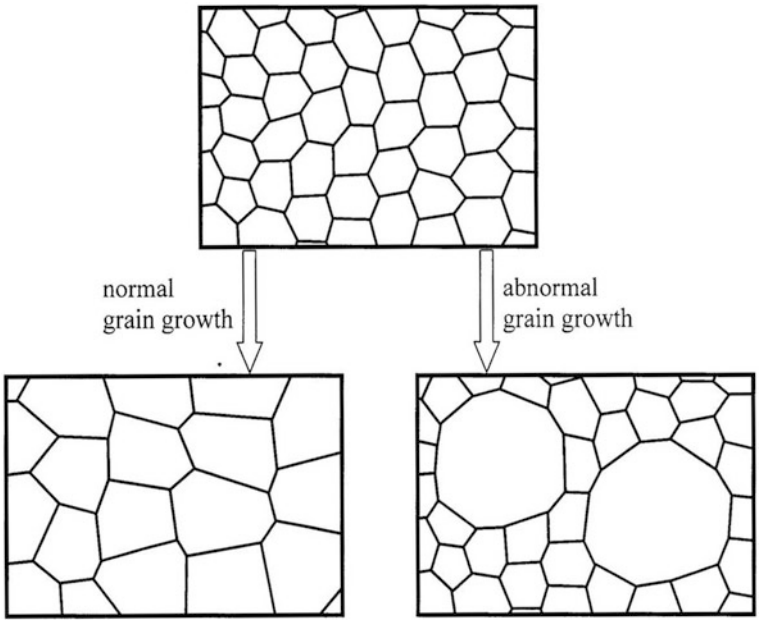

Fig. 2.2 Scheme of normal grain growth and abnormal that (adapted from [1])

severe plastic deformation (SPD) methods, where heating (besides grain growth) is attended with the removal of the crystal lattice micro- and macro distortions, as well as other relaxation effects (see [2, 3] for more details).

The mechanism of the rotational grain growth in NMs is imperfectly studied and therefore some recent investigations in this direction should be marked. It was

shown through using molecular dynamics (MD) simulation that in nanostructures GBs migration and grains rotation can occur simultaneously, especially for small GS [4]. The velocity of grain rotation and its contribution to the general GG became less important as a result of GBs migration, which caused an increase in GS during grain growth. It was also mentioned that the rotation velocity depends on the conjunction geometry of touching grains [5]. By the example of Y_2O_3, it was shown that during the rotation of 20–200 nm grains low-energy/low-angle boundaries are formed in the 600–1000 °C range [6]. An interesting example of a collective grain rotation was observed in TiN and NiO nanocrystalline layers irradiated by high energy Au ions (E = 360 MeV) [7].

2.2 Some Theoretical Approaches and Modeling

As applied specially to consolidated NMs, in order to retard the nanograin growth (and correspondingly to prevent the nanostructure degradation), one can use the following methods: retardation by the second phase inclusions or by pores; change of the initial GS; decrease in the grain mobility by alloying (including segregation formation on GBs) and the decomposition of high-temperature spinodal. The GB migration velocity (v) under the action of own curvature is usually described by the traditional relationship:

$$v = M \cdot P = M_{\mathrm{o}} \exp\left[\frac{-Q_m}{RT}\right] \cdot \frac{2\gamma_{\mathrm{g}}}{r_{\mathrm{g}}}, \tag{2.1}$$

where M is the GBs mobility, M_{o} is a pre-exponential factor, P is the driving force, Q_{m} is the activation energy of the boundary moving process, γ_{g} is the GB energy, and r_{g} is the average grain radius. By convention, the grain retardation process is usually named a *kinetic* approach (when the process is a consequence of the driving force) or a *thermodynamic* one (when it is a result of the driving force decrease at the sacrifice of the GB energy reducing). Theoretically, the both approaches have been derived into a different degree, but the GG retardation due to the micro/nanoinclusions is more widely used in material science. The GG retardation due the inclusions (so-called Zener pinning mechanism) is described by the equation:

$$P_z = \frac{3V_{\mathrm{r}}\gamma_{\mathrm{g}}}{2r_i}, \tag{2.2}$$

where P_{Z} is the Zener drag force and V_{r} is the volume fraction of randomly distributed spherical inclusions with radius r_{i}. It is clear from (2.2) that the effective GG retardation can be achieved by increasing the number of inclusions and/or decreasing their radius.

In the frame of kinetic approach, the influence of nanoinclusions, pores, TJs, and quaternary points on thermal stability was analyzed by Novikov, Shwindlerman et al.

(e.g., [8–12]). From their results, it is worthy to mention that the role of TJs and quaternary points in retardation process can be described by the expression:

$$v = \frac{\gamma_g MK}{1 + 1/\Lambda + 1/\Lambda^*}, \tag{2.3}$$

where K is the GBs curvature, $\Lambda = aM_T/M$, and $\Lambda^* = a^2 M_Q/M$, where a is the spacing between triple lines, and M_T and M_Q are the mobilities of TJs and quaternary points, respectively [11]. The numerical estimations using expression (2.3) have demonstrated [10] that the junction contribution in the nanostructure stabilization increases with decreasing initial GS. It is of interest that the process is especially well detectable at low temperatures, but after heating some inversion is detected and the boundaries with junctions become more mobile.

The thermodynamic analysis allowed determination the sign and value of the TJs linear extension, which was found to be positive and equal to $(6.03 \pm 3.0)\ 10^{-8}$ J/m [12]. It its turn, this value led to a more correct estimation of the GG driving force, and it was shown for Cu that a critical mean GS (below which the TJs values must be properly accounted in the estimation of boundary migration) is about 55 nm.

The numerical models of nanoparticle movement during GBs migration have revealed some dualism in a nanostructure evolution, which consists in the fact that the nanoparticles presence (depending on their volume content and total GBs migration) not only can decrease grain mobility, but also assists its increase leading to an abnormal grain growth [8, 9]. Consideration of various versions for the interaction of pores and GBs has shown that processes of grain growth and pore annihilation under annealing can proceed with different kinetic parameters depending on the component size and mobility [13].

To calculate the GBs mobility, thermodynamic studies of two-component nanosystems were carried out that allowed estimation of ΔG value for alloys with taking into account not only a concentration factor but also the presence of nanograins [14–17]. The key moment in these studies was to apply the well-known regular solution approximation to both bulk and GB regions of nanocrystals. Finally, the equation for the ΔG value took the form [15, 16]:

$$\begin{aligned}\Delta G = {} & (1 - f_b)\,\Delta G_g + f_b \Delta G_b + z\psi f_b \left(X_b - X_g\right) \\ & \left[(2X_b - 1)\omega_b - (zt)^{-1}\left(\Omega^B \gamma_g^B - \Omega^A \gamma_g^A\right)\right],\end{aligned} \tag{2.4}$$

where ΔG_g and ΔG_b are the Gibbs free energies for inner grain regions (g) and GBs those (b); f_b is the volume fracture of GB regions defined by relation:

$$f_b = 1 - \left(\frac{L - t}{L}\right)^3, \tag{2.5}$$

where L is GS; t is the thickness of GB region (usually equals 0.5–1 nm); z is the coordination number for bulk material A; ψ is the fraction of atoms with interatomic

bonds in GBs regions; X_b and X_g are the solute concentrations in the GB and inner regions which must satisfy the condition of the average concentration $X = f_b X_b + (1 - f_b) X_g$; Ω^A and Ω^B are the component atomic volumes of alloy A–B components (addition); γ_g^A and γ_g^A are the partial energies of their GBs; and ω_b is the interaction parameter for the GB regions, used in the regular solution approximation defined as a function of the paired interaction energy (E) by expression:

$$\omega_b = E^{AB} - \frac{E^{AA} + E^{BB}}{2} \tag{2.6}$$

The thermodynamic properties of ΔG surfaces and their minima can be calculated using these equations and varying L values, which allows finding characteristic for the most thermally stable nanoalloys. The different situations of ΔG minimization applied to GG and phase decomposition (variation of content, change in temperature and interaction parameters, absence of ΔG minimum, different combinations of mixing and segregation enthalpies, presence of metastable nanoalloy, formation of two-phase nanocomposites, and so on) were analyzed thoroughly in [16].

Figure 2.3 shows the segregation enthalpy ΔH_S dependence on the mixing enthalpy ΔH_M for various W-based alloys at 1100 °C [15].

The segregation and mixing enthalpies were calculated with the following formulae:

$$\Delta H_S = z\left[\omega_g - 0.5\omega_b - \frac{\left(\Omega^B \gamma_g^B - \Omega^A \gamma_g^A\right)}{2zt}\right] \tag{2.7}$$

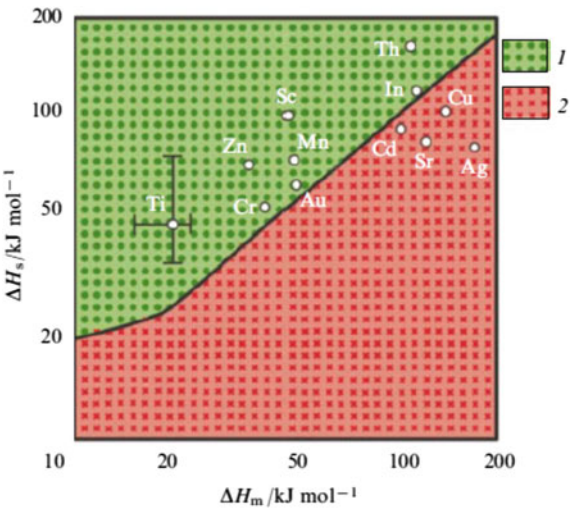

Fig. 2.3 Stability map of tungsten-based alloys at 1100 °C: *1* and *2* are the stability regions of nanocrystalline and CG W alloys, respectively (adapted from [15])

and

$$\Delta H_{\mathrm{M}} = z\omega_g X(1-X), \tag{2.8}$$

where ω_{g} is defined analogously to expression (2.6).

As indicated in Fig. 2.3, the nanocrystalline state is fixed in alloys for which the corresponding points lie above the $\Delta H_{\mathrm{S}} = \mathrm{f}(\Delta H_{\mathrm{M}})$ curve, whereas the CG objects correspond to the bottom part (2) of the diagram.

The same approach-based regular solution approximation for inner and GB regions [14] was used in [17], where the temperature effect was studied in Fe–Zr, Cu–Zr, Cu–Nb, and Ni–W alloys with a varying content of second component. The authors [17] have accounted the role of elastic contribution into the alloy formation in the ΔG calculations (apart from pure chemical interactions). The results showed that the most marked decrease in the grain growth under nanoalloy annealing is observed for zirconium added with small amount of iron.

Another method for GB and inner regions account was developed in [18–20] where authors took into consideration the difference in the excess free volume ΔV between GBs and bulk material. Finally, the relations for estimation of enthalpy H, entropy S and free energy G were derived as follows:

$$H = X_{\mathrm{b}} H_{\mathrm{b}}(\Delta V, T) + (1 - X_{\mathrm{b}}) H_{\mathrm{g}}(T), \tag{2.9}$$

$$S = X_{\mathrm{b}} S_{\mathrm{b}}(\Delta V, T) + (1 - X_{\mathrm{b}}) S_{\mathrm{g}}(T), \tag{2.10}$$

$$G = X_{\mathrm{b}} G_{\mathrm{b}}(\Delta V, T) + (1 - X_{\mathrm{b}}) G_{\mathrm{g}}(T), \tag{2.11}$$

where $\Delta V = [(V_{\mathrm{b}}/V_{\mathrm{g}}) - 1]$, V_{b} and V_{g} are volumes of primitive cells in the GB and inner regions, respectively. The formula for ΔV assumes some excess free volume in the systems due to non-ordered arrangement of atoms in GB regions ($V_{\mathrm{b}} > V_{\mathrm{g}}$). The ΔV values and thermodynamic functions for GB regions (including heat capacity and Debye temperature) are taken with regard to experimental data. The method has been used to estimate the thermal stability and phase transformations of some Sm–Co system compounds, such as $SmCo_5$, Sm_2Co_{17}, $SmCo_7$, etc. [18–22].

The thermodynamic stability of binary nanoalloys was analyzed also by a new Monte-Carlo modeling method [23], where it was proposed to correct the stwo-phase alloys stability map (see Fig. 2.3) by appending two additive regions describing the decomposition of CG alloys and duplex nanoalloys. Other theoretical studies estimated the spinodal decomposition conditions for the Al_2O_3–ZrO_2 and TiN–SiN quasi-binary systems as well as investigated the behavior of interfaces in multi-layer TiN/SiN/TiN nanocomposites [24–28]. In some studies [24–26], the thermodynamic approach was combined with the density function theory (DFT), which allowed calculation not only the thermodynamic characteristics (ΔG, ΔH, etc.), but also the electronic and crystal structure parameters, as well as the material elastic modulus. The calculations revealed that in the metastable TiN–SiN system the dome top of spinodal and bimodal decomposition occurs at about $T \sim 3200$ K,

and below 1273 K the system practically is two-phased [24]. The peculiarities of interface thermal stability in various one-layer TiN/Si_3N_4 structures were investigating in the 0–1400 K range by using the so-called first principles method of MD [27, 28]. In particular, it was marked that the thermal instability of SiN cubic modification can be assigned to the vacancy formation in the silicon sublattice.

At the present time, it is difficult to give preference to any of described theoretical approaches notably, taking into account that the calculations by formulae (2.1–2.11), often are impossible because of the necessary thermodynamic data absence.

Furthermore, there is a general problem of the classical thermodynamics applicability to nanoscale objects. For example, Rusanov [29] supposes that the traditional notions, connected with surface energy, are acceptable as a whole only for isolated nanoparticles sizing over 10 nm. At sizes under 1 nm, any nanoparticle (or nanolayer) practically can acquire the surface properties, i.e., it transforms into a distinctive physical state (distinguished from a volume phase) and this fact requires a special approach. The size range of 1–10 nm is an intermediate one and in each particular case must be considered specially. Another lower limit for nanocrystal sizes was marked by Glezer [30], who pointed that the nanocrystallinity notion disappears with disappearing the symmetry elements characteristic for the given class of crystals. In other words, the meaning and significance of symmetry elements preserve only to the limit when their sizes are commensurable with the three coordination spheres. Then, the minimal critical crystallite size for the body-central cubic (BCC) and face-central cubic (FCC) structures is about 0.5 nm (α-Fe) and 0.6 nm (Ni), respectively. From the above mentioned data, it can be tentatively supposed that the GBs thickness (even with accounting the near boundary regions) is close to the lower limit of the classical thermodynamics applicability. In general, the question of the GB region behavior remains open and requires the further experimental and theoretical studies.

2.3 Main Experimental Results

2.3.1 Bulk Nanomaterials

The thermal stability of consolidated NMs was studied by many authors (see [1, 31–35] and references therein), therefore our attention below will be paid to recent results. Of them, new findings in support for the above described approaches seem to be the most important. In Table 2.1, the experimentally obtained GS values for the Cu–5 at.% Zr alloy samples annealed at 300–700 °C [36] are compared with values calculated by method described in [17]. It is easily seen that the difference is about 4–10 times, but these results can be accepted as satisfactory in regard to the model approximations [17].

Table 2.1 Experimental and calculated values of GS in annealed Cu–5 at.% Zr alloy

T (°C)	Grain size (nm)	
	Experimental values [36]	Calculated values [17]
300	9	35
500	15	55
700	22	230

The suggested presence of the nanocrystalline state in the W–Ti alloy in [15] (see Fig. 2.3) was verified in experiments with the W–20 at.% Ti powder (the initial nanograins size of 20 nm), which practically did not change after weekly annealing at 1100 °C. At the same annealing conditions, the GS in non-doped tungsten was about 600 nm [15, 37].

Thus, the developed theoretical methods [14–17] are acceptable for estimation of the metallic nanoalloy thermal stability. It is also important that the possible existence of W–20 at.% Ti alloys in a nanocrystalline state has been independently predicted by the Monte-Carlo calculations [37]. The study of titanium distribution in W–20 at.% Ti alloys nanostructure revealed its heterogeneous character because of the content variations in the range from 0 to 50 at.% [15, 37], i.e., under the considered conditions the alloy thermal stability can be explained not only by the free energy decrease, but also by the appearance of segregation inclusions and Zener pinning mechanism. The same situation (i.e., with the action of two mechanisms) can take place in the Cu–5 at.% Zr alloy annealed at 700 °C, when difference between the experimental and theoretical GS values (based on accounting one mechanism) was maximal (see Table 2.1).

To compare experimental findings of different studies concerning the effectiveness and congruence of both the kinetic and thermodynamic approaches for description of nanograin thermal growth retardation, the corresponding data were normalized to the melting temperature T_m in the homological temperature scale by Koch et al. [38]. From the other side, only the results for systems with a GS of under 100 nm in annealed samples were taken in account in [38]. Its authors only used most reliable data provided by TEM and XRD methods. The alloy-based Al, Mg, Cu, and Fe samples with nanoinclusions of Al_2O_3, AlN, ZrO_2, and Nb proved to be thermally stable at high homological temperatures up to (0.75–0.85) T_m, whereas the alloy-based Ni, Co, Fe, Y, RuAl, and TiO_2 systems with additions of W, P, Zr, Fe, and Ca exhibited lower thermal stability up to (0.35–0.65) T_m.

High thermal stability was fixed for copper alloys with tungsten and tantalum additives (10 at.%), prepared by a high-energy milling at cryogenic temperature of the initial powders with their following pressing and sintering [39, 40]. In other experiments, the initial GS of Cu–W alloys was of $\sim$15 nm, but after annealing the grains had L of $\sim$60 nm [37]. In Table 2.2, the results of more detailed investigation of the Cu–Ta alloys are presented. They show a high enough thermal stability of the objects.

For comparison, it is worthy to mark that the microhardness of Cu–10 at.% W alloys in the initial and annealed states equals about 3–2.6 GPa, correspondingly [38], i.e., it is lower than the values obtained in [40] (see Table 2.2). After detailed

Table 2.2 Evolution of GS and microhardness after annealing Cu–10 at.% Ta under pure H_2 gas (for 4 h) (adapted from [40])

Annealing temperature		Grain size (nm)		Microhardness (GPa)
(°C)	(T/T_m)	Cu phase	Ta phase	
20	0.22	6.7	6	4.8
540	0.6	21 ± 4	22 ± 5	~3.6
770	0.77	54 ± 9	37 ± 9	n/d
900	0.87	111 ± 26	42.5 ± 25	3.4
1040	0.97	167 ± 50	99 ± 99	2.6

consideration of different mechanisms of thermal stability connected with TJs, doping, inclusions, segregations, etc., the authors [40] made a conclusion that the observed high thermal stability of such Cu–Ta alloys was connected with the formation and following decomposition of tantalum segregations at the GB regions, i.e., with some combined action of the thermodynamic and kinetic mechanisms. The latter comes at high temperatures as a result of the GB layer decomposition into inclusions (nanoclusters by terminology of authors [40]), which retards GG within a high temperature interval. This conclusion was verified by the MD calculations and sample structure experimental studies using TEM [41].

A significant role of the kinetic mechanism in the thermal stability due to the retarding action of the nanoinclusions was marked also for the Cu–Nb, Ni–Y, and Fe–Zr nanoalloys [42–44], but was not observed for Cu–Fe and Pd–Zr systems [43, 44]. The thermal stability of Cu-based nanoalloys is thoroughly considered in survey [35].

In addition to the above mentioned doping and inclusions, interfaces also retard grain growth, which can be adjusted during the NMs manufacturing processes. Figure 2.4 shows the temperature dependences of basic parameters, such as GS, lamellar spacing width, and hardness for copper samples prepared by both traditional methods of SPD and magnetron sputtering with the nanotwinned structure formation [45].

Here, one can see very weak changes in the lamellar thickness and high hardness for nanotwinned samples in distinction to the usual sufficient GS growth and hardness decrease with temperature for the common type nanostructures. This high thermal stability of the low-angle nanotwinned boundaries is related to their low GB energy, which is lower than that of ordinary high-angle boundaries by an order of magnitude. It is worthy to mention that the high electrical conductivity and wear resistance of such copper samples with a nanotwinned structure [46] is very important for various applications. Such advantages were described for nickel [47] and Cu–Nb nanocomposites [48] as well.

Let us notice that there are many situations when GG (in particular, an abnormal grain growth; see Fig. 2.2) in NMs cannot be prevented even at room temperature. The kinetics curves of the GG in nanocrystalline palladium at 20 °C are presented in Fig. 2.5, where coincidence of the experimental [49] and calculated [50] results seems satisfactory up to the beginning of abnormal grain growth (at a test duration

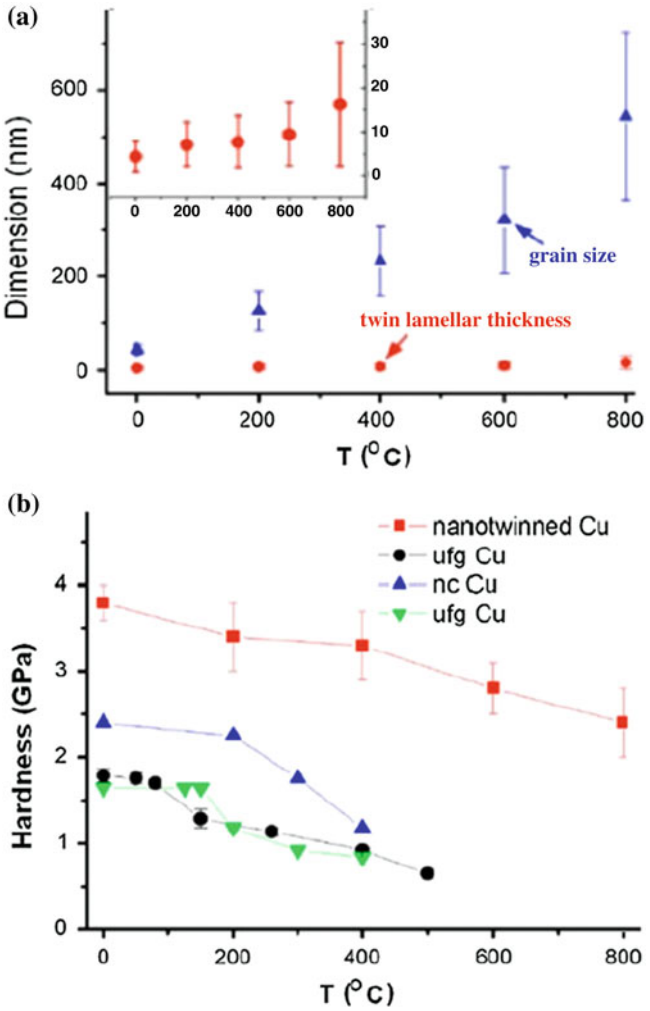

Fig. 2.4 The effect of the annealing temperature on the twin lamellar thickness and GS (**a**) as well as hardness (**b**) of sputtered nanotwinned Cu films and other, more traditionally prepared, ultrafine-grained (ufg)/nanocrystalline (nc) Cu specimens (adapted from [45]). The *inlet* shows the lamellar thickness change

of over 8 h). On the other hand, when the TJs retardation action is not taken into account, the discrepancy between theory and experiment becomes very striking. But neither the presence of many TJs nor the existence of residual pores (the initial GS was of $\sim$5 nm and the porosity was of $\sim$4 %) and admixtures (0.4 at.% H, 0.2 at.% N and 0.1 at.% O) can not prevent the abnormal grain growth, which leads to the transformation of the palladium nanostructure into ordinary microstructure with GS about $\sim$10 μm after 2-month exposition at room temperature [49].

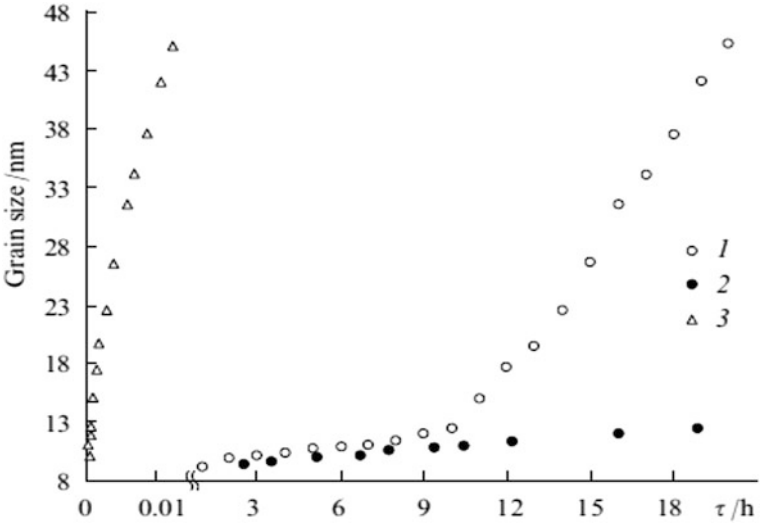

Fig. 2.5 Room temperature grain growth in nanocrystalline Pd: (*1*) Experimental results [49]; (*2* and *3*) calculated values with and without considering the TJs drag effect, respectively (adapted from [50])

An abnormal grain growth at high and room temperatures was observed in a number of experiments, including the TEM studies in situ [40, 53–55] for many other materials-based copper [40, 51], nickel [52–54], iron [55, 56], hard WC–Co alloys [57], and diamond [58]. It is worthy to notice that the listed materials were manufactured by various methods: the pulsing electrical deposition [54], pressing and sintering [49, 57], high-pressure torsion (HPT) at liquid nitrogen temperature [51], pulsing laser deposition [58, 59], intensive mechanical treatment (milling + mixing) or mechanical alloying (MA) [40, 55, 56], and sintering under high pressure (T = 1400 °C, P = 6.8 GPa) [58]. Naturally, the experiments with such wide diversity of objects and methods have revealed some new peculiarities in the initial and final states of material. In particular, the in situ TEM studies of nickel films made it possible to fix numerous defects in annealed samples, such as the presence of stacking-fault tetrahedra (SFT) and dislocation loops as well as the low-energetic TB formation [53, 54]. The authors [51] have revealed non-stability of copper nanostructure at room temperature and made a conclusion that the plastic deformation method at low temperatures is unpromising for NMs manufacture. The study in situ of the $Fe_{91}Ni_8Zr_1$ alloy thermal stability has shown that the abnormal grain growth begins above 700 °C and is related to the formation of γ-phase crystals with a FCC structure [56].

There are many new interesting findings concerning theoretical description of abnormal grain growth partially given above in Sect. 2.2 [8–10] and also in [59, 60], but the principal aspects of this effect are still to be solved (e.g., the role of defects and admixtures, prediction of change in the grain growth mechanism from

normal to abnormal one, etc.). In conclusion of this subsection, it is worthy to mark that the recent studies of the nanoglass behavior under heating (for the Fe–Sc system samples) have revealed a relaxation process and some redistribution of excess free volume [61].

2.3.2 *Nanostructured Films and Coatings*

Above, some results have been presented demonstrating a high thermal stability of films with a nanotwinned structure and high-temperature nanocomposites (Fig. 2.4 [45] and [24–28]), but films and coatings themselves represent a very interesting and important field of investigations. Such nano-objects have been studied before (see [62–67] and references therein), but it is evident that they merit a more detailed consideration as convenient objects to get new important data. For example, the studies of one-/multi-layer nitride and nitride/carbide/boride films have already revealed a new class of superhard coating materials with hardness at the level of diamond and boron nitride (BN) (Table 2.3).

The results presented in Table 2.3 were obtained contemporaneously and independently of one another by investigators in many countries (USA, Sweden, former USSR, Austria, and Germany), and they all demonstrated the films high thermal stability as well as a role of the high-temperature spinodal decomposition in the nitride solid solutions. Figure 2.6 reveals that the thermal stability of new materials surpasses that of diamond, amorphization of which begins at ~800 °C. Also, it was found that the high thermal stability of (Ti, Zr)N films is connected with spinodal decomposition in the TiN–ZrN system with the nanocrystalline structure formation.

Table 2.3 Some first results for superhard films (adapted from [64])

Films	Microhardness (GPa)	Year	Authors[a]
One-layer films			
$Ti(B, C)_X$	~70	1990	Knotek et al.
$Ti(B, N)_X$	~60	1990	Mitterer et al.
B_4C	50–70	1992	Veprek
Multi-layer films			
TiN/VN	54	1987	Helmerson et al.
TiN/NbN	~78	1992	Andrievski et al.
TiN/NbN	48	1992	Shinn et al.
TiN/ZrN	~70	1992	Andrievski et al.

[a]See [64]

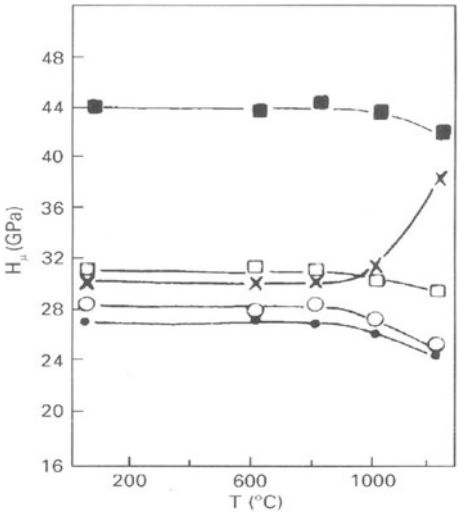

Fig. 2.6 The temperature effect on microhardness 2 μm thick nitride films. ● one-layer ZrN; ○ one-layer TiN; **x** solid solution (Ti, Zr)N disintegrated above 800 °C; □ TiN/ZrN (10 layers); ■ TiN/ZrN (20 layers) (adapted from [64])

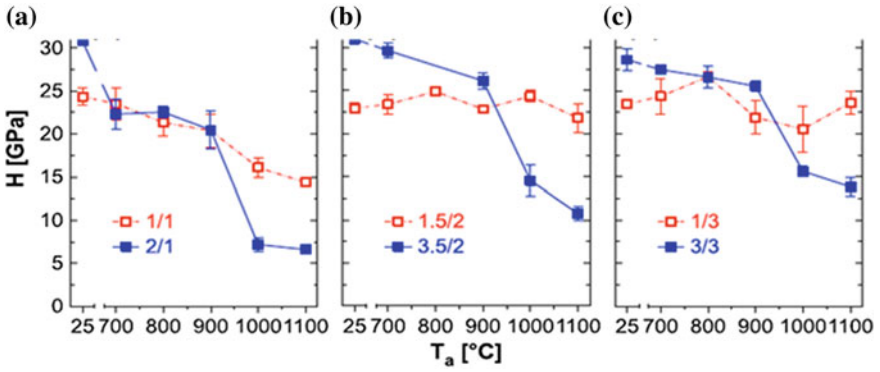

Fig. 2.7 The temperature effect on microhardness of CrN/AlN films with different thickness of individual layers: **a** 1 nm, **b** 2 nm, and **c** 3 nm thin AlN layers combined with CrN layers thicknesses of (**a**) 1 and 2 nm, (**b**) 1.5 and 3.5 nm, and (**c**) 1 and 3 nm (adapted from [68])

By now, new and more thermally stable films and coatings have been synthesized. For example, Fig. 2.7 demonstrates the temperature-microhardness dependences for CrN/AlN multi-layer films with varying layers thickness [68]. These results obviously indicate that the films with the AlN layers predomination (1.5/2 and 1/3) preserve their hardness after annealing at 1100 °C. The TEM and XRD studies allow suggesting that it is connected with a greater preservation of the

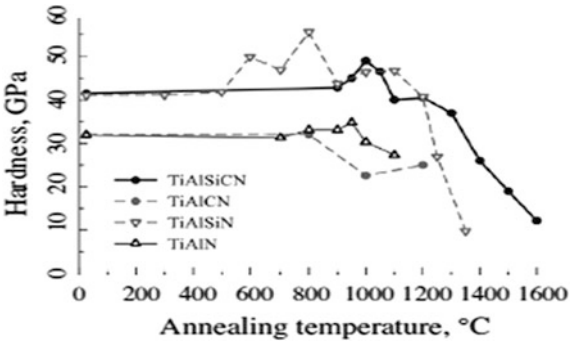

Fig. 2.8 The temperature effect on hardness of the TiAlN, TiAlSiN, TiAlCN, and TiAlSiCN coatings (adapted from [69])

dissociating chromium nitride. In the experiments, the number of individual layers was changing from 250 to 580 (with the same common film width about 1.5 μm).

The examination of the one-layer TiAlSiCN coatings after vacuum annealing in the 900–1600 °C range showed that the high initial hardness (~42 GPa) changes very little after annealing at 1300 °C with a "comb" like nanocomposite structure preservation (Fig. 2.8) [69].

A high thermal stability after annealing in the 1000–1300 °C range was found for the superhard nitride coatings-based high-entropy multicomponent Ti–Hf–Zr–V–Nb alloys [70]. Now, it is evident that the evolution of high-temperature structure and properties of these multicomponent nanostructured coatings are defined by many various factors connected with relaxation, recrystallization, diffusion, and other processes, and we are only at the pioneering stage of such studies (e.g., [69, 71, 72]).

2.4 Examples of Application

Today, the NMs high-temperature application can be realized predominantly as films/coatings-based HMPC used for tools or friction units. As for the development of tool NMs, Veprek's paper [73] devoted to search for new superhard materials was of a great value. It was published more than 15 years ago and had a great resonance (its citation index CI is over 860).

The proposed *nc*-(Al, Ti)N/*a*-Si_3N_4 composite coatings-based (Al, Ti)N nanocrystallites in an amorphous matrix of silicon nitride exhibiting high hardness, wear and oxidation resistances (Fig. 2.9) were realized in industry applications and repeatedly improved [67, 74]. An optimal thickness of Si_3N_4 is now considered to be about 0.3 nm (1 layer) [67].

In general, the main demands for tool materials can be formulated as follows: the hardness and strength must be preserved at high temperatures, as well as the wear, oxidation, and friction resistances. These characteristics were realized in the above mentioned study of Shtansky et al. [69] by the example of TiSiCN coatings with Al

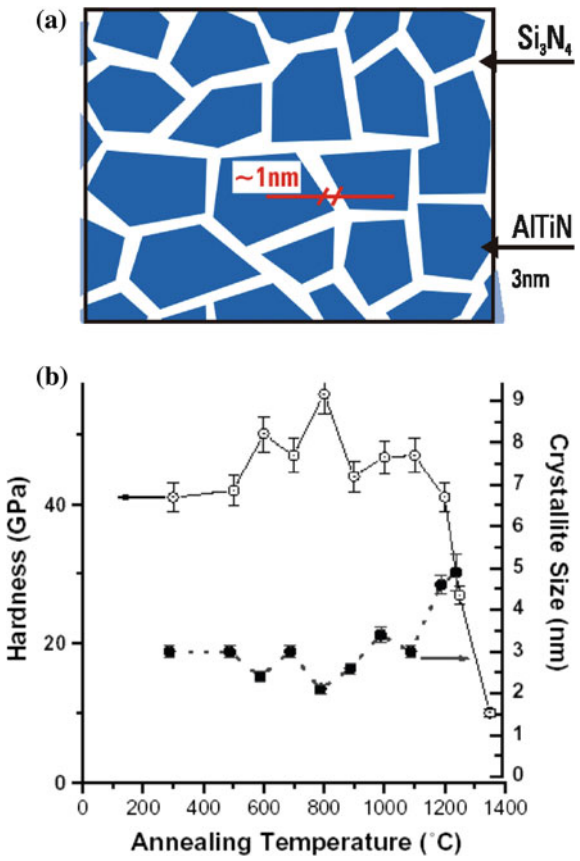

Fig. 2.9 Scheme of the *nc*-(Al, Ti)N/*a*-Si_3N_4 nanostructure (**a**) and the temperature evolution of its hardness and crystallite size (**b**) (adapted from [75, 76])

and Cr additions (see Fig. 2.8). A comparison of the thermal and oxidation stability for various one-layer boron-nitride coatings (Ti–B–N, Ti–Cr–B–N, Ti–Si–B–N, and Ti–Al–Si–B–N) was carried out in [77]. Some other combinations of extreme actions including high temperatures, irradiation, deformation, and corrosion effects will be described in the next Chaps. 3–5.

It is important to mark that various methods for manufacturing thermally stable nanostructures [78, 79] are widely studied and carefully examined especially to produce the materials-based steels, titanium, etc., generally used in machine construction. As an example, to improve nanostructured stainless steel 316L, such modern methods as HPT, equal channel angular pressing (ECAP), surface mechanical attrition treatment (SMAT) and fast multiple rotation rolling (FMRR) are used [78].

The intensive searches for rise in the NMs thermal stability are in progress, and new practically important materials (such as alloys of Al, Mg, Ti, Cu, Ni, Fe, Nb, Mo, and W as well as Ti and Sn oxides, silicon carbides, etc.) and results should be forthcoming, particularly in manufacturing electric contacts, refractory items,

high-temperature sensors, etc. The GB engineering approach as applied to Ni–Fe-based superalloy 706 has been described by Detor et al. [80], but this study was realized only for CG objects and NMs approach still waits for its realization.

Different models of the thermodynamic GS stabilization in many metallic alloys reviewed and compared in an overview [81]. High thermal stability of superhard nanostructured lamellar (Ti, Zr)C was described in [82].

References

1. Koch CC, Ovid'ko IA, Seal S et al (2007) Structural nanocrystalline materials: fundamentals and applications. Cambridge University Press, Cambridge
2. Estrin Y, Vinogradov A (2013) Extreme grain refinement by severe plastic deformation: a wealth of challenging science. Acta Mater 61:782–817
3. Valiev RZ, Zhilyaev AP, Langdon TG (2014) Bulk nanostructured materials: fundamentals and applications. Wiley, Weinheim
4. Upmanyu M, Srolovitz DJ, Lobkovsky AE et al (2006) Simultaneous grain boundary migration and grain rotation. Acta Mater 54:1707–1715
5. Bernstein N (2008) The influence of geometry on grain boundary motion and rotation. Acta Mater 56:1106–1113
6. Chaim R (2012) Groan coalescence by grain rotation in nanoceramics. Scr Mater 66:269–271
7. Zizak I, Darowski N, Klaumünzer S et al (2009) Grain rotation in nanocrystalline layers under influence of swift heavy ions. Nucl Instr Meth Phys Res B 267:944–948
8. Novikov VY (2010) On grain growth in the presence of mobile particles. Acta Mater 58:3326–3331
9. Novikov VY (2012) Microstructure evolution during grain growth in materials with disperse particles. Mater Lett 68:413–415
10. Novikov VY (2008) Impact of grain boundary junctions on grain growth in polycrystals with different grain sizes. Mater Lett 62:2067–2069
11. Gottstein G, Shvindlerman LS (2005) A novel concept to determine the mobility of grain boundary quadruple junctions. Scr Mater 52:863–866
12. Zhao B, Gottstein G, Shvindlerman LS (2011) Triple junction effects in solids. Acta Mater 59:3510–3518
13. Klinger L, Rabkin E, Shvindlerman LS et al (2008) Grain growth in porous two-dimensional nanocrystalline materials. J Mater Sci 43:5068–5075
14. Trelewicz JR, Schuh CA (2009) Grain boundary segregation and thermodynamically stable binary nanocrystalline alloys. Phys Rev B 79:094112 (1–13)
15. Chookajorn T, Murdoch HA, Schuh CA (2012) Design of stable nanocrystalline alloys. Science 337:951–954
16. Murdoch HA, Schuh CA (2013) Stability of binary nanocrystalline alloys against grain growth and phase separation. Acta Mater 61:2121–2132
17. Saber M, Kotan H, Koch CC et al (2013) Thermodynamic stabilization of nanocrystalline binary alloys. J Appl Phys 113:063515 (1–10)
18. Xu WW, Song XY, Li ED et al (2009) Thermodynamic study on phase stability in nanocrystalline Sm–Co alloy system. J Appl Phys 105:104310 (1–6)
19. Song X, Lu N, Huang Ch et al (2010) Thermodynamic and experimental study on phase stability in nanocrystalline alloys. Acta Mater 58:396–407
20. Xu W, Seng X, Zhang Z (2010) Thermodynamic study on metastable phase: from polycrystalline to nanocrystalline system. Appl Phys Lett 97:181911 (1–3)

21. Xu W, Song X, Lu N et al (2009) Nanoscale thermodynamic study on phase transformation in the nanocrystalline Sm_2Co_{17} alloy. Nanoscale 1:238–244
22. Xu W, Song X, Zhang ZX (2012) Multiphase equilibrium, phase stability and phase transformation in nanocrystalline alloy systems. Nano Brief Rep Rev 7:125012 (1–10)
23. Chookajorn T, Schuh CA (2014) Thermodynamics of stable nanocrystalline alloys. Phys Rev B 89:064102 (1–10)
24. Zhang RF, Veprek S (2008) Phase stability of self-organized nc-TiN/a-Si_3N_4 nanocomposites and of $Ti_{1-x}Si_xN_y$ solid solution studied by *ab initio* calculation and thermodynamic modeling. Thin Solid Films 516:2264–2275
25. Sheng SH, Zhang RF, Veprek S (2011) Phase stabilities and decomposition mechanism in the Zr–Si–N system studied by combined ab initio DFT and thermodynamic calculation. Acta Mater 59:297–307
26. Sheng SH, Zhang RF, Veprek S (2011) Study of spinodal decomposition and formation of nc-Al_2O_3/ZrO_2 nanocomposites by combined ab initio density functional theory and thermodynamic modeling. Acta Mater 59:3498–3509
27. Ivashchenko VI, Veprek S, Turchi PEA et al (2012) Comparative first-principles study of TiN/SiN_x/TiN interfaces, Phys Rev B 85:195403 (1–14)
28. Ivashchenko VI, Veprek S, Turchi PEA et al (2012) First-principles study of TiN/SiC/TiN interfaces in superhard nanocomposites. Phys Rev B 86:014110 (1–8)
29. Ivashchenko VI, Veprek S (2013) First-principles molecular dynamics study of the thermal stability of the BN, AlN, SiC and SiN interfacial layers in TiN-based heterostructures: comparison with experiments. Thin Sol Films 545:391–400
30. Rusanov AI (2002) The surprising world of nanostructures. Russ J Gen Chem 72:495–512
31. Glezer AM (2002) Amorphfnye i nanocrystallicheskie struktury: skhodstvo, razlichiya ivzaimnye perekhody (Amorphous and nanocrystalline structures: similarity, differences, and mutual transitions). Ros Khim Zhurn 46(5):57–64 (in Russian)
32. Ovid'ko IA (2009) Theories of grain growth and methods of its suppression in nano- and polycrystalline materials. Mater Phys Mech 8:174–199
33. Castro RHR (2013) On the thermodynamic stability of nanocrystalline ceramics. Mater Lett 96:45–56
34. Andrievski RA (2014) Review of thermal stability of nanomaterials. J Mater Sci 49:1449–1460
35. Tschopp MA, Murdoch HA, Kecskes LJ et al (2014) "Bulk" nanocrystalline metals: review on the current state of the art and future opportunities for copper and copper alloys. JOM 66:1000–1019
36. Atwater MA, Scattergood RO, Koch CC (2013) The stabilization of nanocrystalline copper by zirconium. Mater Sci Eng A 559:250–256
37. Chookajorn T, Schuh CA (2014) Nanoscale segregation behavior and high-temperature stability of nanocrystalline W–20 at%Ti. Acta Mater 73:128–138
38. Koch CC, Scattergood RO, Saber M et al (2013) High temperature stabilization of nanocrystalline grain size: thermodynamic versus kinetic strategies. J Mater Res 28:1785–1791
39. Atwater MA, Roy D, Darling KA et al (2012) The thermal stability of nanocrystalline copper cryogenically milled with tungsten. Mater Sci Eng A 558:226–233
40. Darling KA, Roberts AJ, Mishin Y et al (2013) Grain size stabilization of nanocrystalline copper at high temperature by alloying with tantalum. J All Comp 573:142–150
41. Frolov T, Darling KA, Kecskes LJ et al (2012) Stabilization and strengthening of nanocrystalline copper by alloying with tantalum. Acta Mater 60:2158–2168
42. Özerinç S, Tai K, Vo NQ et al (2012) Grain boundary doping strengthens nanocrystalline copper alloys. Scr Mater 67:720–723
43. Koch CC, Scattergood RO, VanLeeuwen BK et al (2012) Thermodynamic stabilization of grain size in nanocrystalline metals. Mater Sci Forum 715–716:323–328
44. Darling KA, Kecskes LJ, Atwater M et al (2013) Thermal stability of nanocrystalline nickel with yttrium additions. J Mater Res 28:1813–1819

45. Anderoglu O, Misra A, Wang H et al (2008) Thermal stability of sputtered Cu films with nanoscale growth twins. J Appl Phys 103:094322 (1–6)
46. Lu L, Shen Y, Chen X et al (2004) Ultrahigh strength and high electrical conductivity in copper. Science 304:422–426
47. Liu X, Zhang HW, Lu K (2013) Strain-induced ultrahard and ultrastable nanolaminated structure in nickel. Science 342:337–340
48. Zheng S, Beyerlein IJ, Carpenter JS et al (2013) High-strength and thermally stable bulk nanolayered composites due to twin-induced interfaces. Nature Commun 4:1696–1703
49. Ames M, Markmann J, Karos R et al (2008) Unraveling the nature of room temperature grain growth in nanocrystalline materials. Acta Mater 56:4255–4266
50. Gottstein G, Shvindlerman LS, Zhao B (2010) Thermodynamics and kinetics of grain boundary triple junctions in metals: recent developments. Scr Mater 62:914–917
51. Konkova T, Mironov S, Korznikov A et al (2010) Microstructure instability in cryogenically deformed copper. Scr Mater 63:921–924
52. Cheng L, Hibbard GD (2008) Abnormal grain growth via migration of planar growth interfaces. Mater Sci Eng A 492:128–133
53. Hattar K, Follstaedt DM, Knapp JA et al (2008) Defect structures created during abnormal grain growth in pulsed-laser deposited nickel. Acta Mater 56:794–801
54. Kacher J, Robertson IM, Nowell M et al (2011) Study of rapid grain boundary migration in a nanocrystalline Ni thin film. Mater Sci Eng A 528:1628–1635
55. Paul H, Krill CE III (2011) Abnormally linear grain growth in nanocrystalline Fe. Scr Mater 65:5–8
56. Kotan H, Darling KA, Saber M et al (2013) An in situ experimental study of grain growth in a nanocrystalline $Fe_{91}Ni_6Zr_1$ alloy. J Mater Sci 48:2251–2257
57. Mannesson K, Jeppsson J, Borgenstam A et al (2011) Carbide grain growth in cemented carbides. Acta Mater 59:1912–1923
58. McKie A, Herrmann M, Sigalas I et al (2013) Suppresion of abnormal grain growth in fine grained polycrystalline diamond materials (PCD). Int J Refr Met Hard Mater 41:66–72
59. Novikov VY (2011) On abnormal grain growth in nanocrystalline materials induced by small particles. Int J Mater Res 4:446–451
60. Novikov VY (2013) Grain growth suppression in nanocrystalline materials. Mater Lett 100:271–273
61. Franke O, Leisen D, Gleiter H et al (2014) Thermal and plastic behavior of nanoglasses. J Mater Res 29:1210–1216
62. Hultman L, Mitterer C (2006) Thermal stability of advanced nanostructured wear resistant coatings. In: Cavaleiro A, De Hosson JT (eds) Nanostructured coatings. Springer, New York, pp 609–656
63. Mayrhofer PH, Mitterer C, Hultman L et al (2006) Microstructural design of hard coatings. Progr Mater Sci 51:1032–1114
64. Andrievski RA (2007) Nanostructured superhard films as typical nanomaterials. Surf Coat Technol 201:6112–6116
65. Levashov EA, Shtansky DV (2007) Multifunctional nanostructured films. Russ Chem Rev 76:463–470
66. Pogrebnjak AD, Shpak AP, Azarenkov NA et al (2009) Structures and properties of hard and superhard nanocomposite coatings. Phys-Usp 52:29–54
67. Veprek S (2013) Recent search for new superhard materials: Go nano! J Vac Sci Technol A 31:050822 (1–33)
68. Schlögl M, Paulitsch J, Mayrhofer PH (2014) Thermal stability of CrN/AlN superlattice coatings. Surf Coat Technol 240:250–254
69. Kuptsov KA, Kiryukhantsev-Korneev PhV, Sheveyko AN et al (2011) Structural transformation in TiAlSiCN coatings in the temperature range 900–1600 °C. Acta Mater 83:408–418

70. Firstov SA, Gorban' VF, Danilenko NI et al (2014) Thermal stability of ultrahard nitride coatings from high-entropy multicomponent Ti–V–Zr–Nb–Hf alloy. Powd Metall Met Ceram 52(9–10):560–566
71. Shtansky DV, Kuptsov KA, Kiryukhantsev-Korneev PhV et al (2012) High thermal stability of TiAlSiCN coatings with "comb" like nanocrystalline structure. Surf Coat Technol 206:4840–4849
72. Pogrebnjak AD (2013) Structure and properties of nanostructured (Ti–Hf–Zr–V–Nb)N coatings. J Nanomater 2013:780125 (1–12)
73. Veprek S (1999) The search for novel superhard materials. J Vac Sci Technol A Vac Surf Films 17:2401–2420
74. Veprek S, Veprek-Hejman MJG (2008) Industrial applications of superhard nanocomposites coatings. Surf Coat Technol 202:5063–5073
75. Veprek S, Argon AS (2002) Towards the understanding of mechanical properties of super- and ultrahard nanocomposites. J Vac Sci Technol B 20:650–664
76. Männling H-D, Patil DS, Moto K et al (2001) Thermal stability of superhard nanocomposites coatings consisting immiscible nitrides. Surf Coat Technol 146–147:263–267
77. Kiryukhantsev-Korneev PhV, Shtansky DV, Petrzhik MI et al (2007) Thermal stability and oxidation resistance of Ti–B–N, Ti–Cr–B–N, Ti–Si–B–N, and Ti–Al–Si–B–N films. Surf Coat Technol 201:6143–6147
78. Chui P, Sun K (2014) Thermal stability of a nanostructured layer on the surface of 316L stainless steel. J Mater Res 29:556–560
79. Wang Q, Yin Y, Sun Q et al (2014) Gradient nano microstructure and its formation in pure titanium produced by surface rolling treatment. J Mater Res 29:569–577
80. Detor AJ, Deal AD, Hanlon T (2012) Grain boundary engineering alloy 706 for improved high temperature performance. In: Huron ES, Reed RC, Hardy Mc et al (eds), Superalloys 2012: 12th international symposium on superalloys, TMS, Wiley, Hoboken, pp 873–880
81. Saber M, Koch CC, Scattergood RO (2015) Thermodynamic grain size stabilization models: an overview. Mater Rev Lett 3:65–75
82. Ma T, Hedström P, Ström V et al (2015) Self-organizing nanostructured lamellar (Ti, Zr)C—a superhard mixed carbide. Int J Refr Met Hard Mater 51:25–28